Pinning Properties of Commercial Nb-Ti Wires Described by a 2-Components Model

Luigi Muzzi, Gianluca De Marzi, Chiarasole Fiamozzi Zignani, Luigi Affinito, Mathieu Napolitano, Rosario Viola, César Octavio Domínguez, Luca Bottura, Sandrine Le Naour, David Richter, and Antonio della Corte

***Abstract*—We report on the magnetic and transport characterization of different NbTi commercial strands, carried out at variable temperature and magnetic field. From the critical current densities extracted from transport measurements and magnetization cycles we were able to calculate the normalized bulk pinning forces. The curves show good temperature scaling throughout the explored temperature range, and the reduced pinning force can be described by a simple two-components model system. The extension of the 2-components description of the pinning force to an expression for the critical current density gives a very good agreement with experimental measurements over the whole explored B, T range. The model works for all investigated samples, which are different in size, Cu:nonCu ratios, filament diameters and layouts. These results suggest that pinning mechanisms in conventional NbTi strands should be revised, since Nb-Ti composition gradients and grain boundaries seems to play a not negligible role.**

***Index Terms*—Critical current density, magnetic characterization, superconducting NbTi strands, transport measurements.**

I. Introduction

INDUSTRIAL production of NbTi multi-filamentary strands is capable to achieve very reproducible current densities over long lengths. For this reason design and manufacture of superconducting magnets for various applications, which can range from laboratory test magnets up to large coils as in fusion tokamak reactors or in high energy physics accelerators, have been and still are widely based on this technology.

Identifying pinning centers and pinning mechanisms is of major importance for understanding the behavior of high critical current NbTi wires. On one side, this is fundamental in order to provide a reliable prediction of their performances in relevant operating conditions, on the other side it might open further scenarios for the optimization of wire performances in specific B, T ranges.

In this study we present the results of a measurement campaign carried out on NbTi wires.

Manuscript received October 20, 2009.Current version published February 08, 2010.

L. Muzzi, G. De Marzi, C. Fiamozzi Zignani, L. Affinito, M. Napolitano, R. Viola, and A. della Corte are with ENEA, Frascati Research Center, I-00044 Frascati, Italy (e-mail: gianluca.demarzi@enea.it).

C. O. Domínguez was with ENEA, Frascati Research Center, I-00044 Frascati, Italy. He is now with CERN, Geneva CH-1211, Switzerland (e-mail: octavio.dominguez@cern.ch).

L. Bottura, S. Le Naour, and D. Richter are with CERN, Geneva CH-1211, Switzerland (e-mail: luca.bottura@cern.ch).

Color versions of one or more of the figures in this paper are available online at http://ieeexplore.ieee.org.

Digital Object Identifier 10.1109/TASC.2009.2039124

TABLE I
General Characteristics of the Studied NbTi Strands

Sample name	*Producer*	*Cu:SC*	*Outer diameter (mm)*	*d (μm)* [a]	d_{eff} *(μm)* [b]
Alst564	Alstom	1.55	0.810	20	22
IBA01	Alstom	1.67	0.738	n/a	4.5
ICB01	Bochvar	1.36	0.736	9.8	9.7
ITER-PF	Luvata	1.6	0.718	6	8.2
JT-60SA	Luvata	1.86	0.810	20	15
LUV-NMR	Luvata	6.7	0.710	26	30

[a] Nominal filament diameter.

[b] Effective filament diameter, at 4.2 K.

This large amount of data collected for different NbTi strands can be useful as a basis for a re-examination of the flux pinning in those wires, and to frame it into a phenomenological model system, which can then be used to predict the strand behavior—in terms of critical current density as a function of applied field and temperature, $\mathrm{J_c(B,T)}$—over a large B-T range.

II. Samples

We characterized six NbTi strands with different layouts (Cu:nonCu ratio, strand and filament diameters, inter-strand resistive barrier), produced by Alstom (France), Luvata (Italy), and Bochvar (Russia), by means of transport and magnetic measurements.

Sample characteristics are resumed in Table I. The JT-60SA and Alst564 strands have been designed for the JT-60SA Toroidal Field coils project [1]. In particular, for the case of the JT-60SA magnet project, ENEA had assigned LUVATA Fornaci di Barga the task to produce the strands and to perform the cabling of the NbTi qualification sample, which has been successfully tested at the CRPP SULTAN facility [2].

The IBA01, ICB01 strands (delivered by CERN within the scope of an ITER R&D task [3]), and ITER-PF strands are of relevance for the ITER production of superconductors for the Poloidal Field coils; in particular, the ICB01 belongs to the batch of strands used in the production of the cable for the PF Conductor Insert Coil, recently tested at JAEA-Naka [4]. In Table I, the Cu:nonCu ratios, λ, are reported for each measured wire, along with those for d_{eff}. A sample with high Cu:nonCu ratio (λ) has been also considered (Luv-NMR) in order to study the impact of λ on the strand performances. Also, as shown in Table I, a quite large range of filament diameter values has been explored.

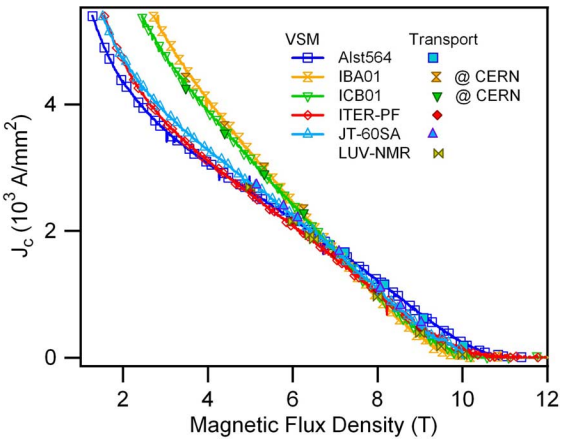

Fig. 1. Critical current densities as a function of applied field for several NbTi strands, at $\mathrm{T} = 4.2$ K. Closed symbols represent transport $\mathrm{J_c^{transp}}$, whereas open symbols represent the $\mathrm{J_c^{magn}}$ extracted from the magnetization loops.

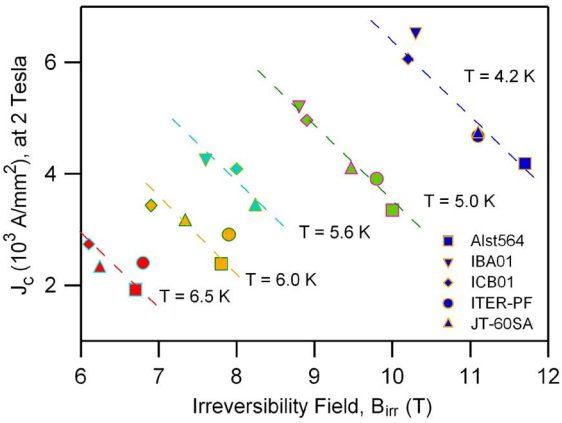

Fig. 2. $\mathrm{J_c(2\,T)}$ as a function of the experimental irreversibility fields for the whole dataset but LUV-NMR, at different temperatures. Lines represent a guide for the eyes.

III. Experimental Details

Critical current densities, $\mathrm{J_c(T,B)}$, have been measured by using the Variable Temperature Insert (VTI) facility developed at ENEA, which comprise a 47 mm-bore superconducting magnet (background magnetic field up to 12.5 T) and a helium gas-flow cryostat, which allows to collect data with an overall error bar of ± 10 mK. Details about the test facility can be found in [5]. Three of the six studied samples have also been measured at CERN, at 4.2 K and 1.9 K, using the method and procedure described in [6]. The measurements cover a field range up to 6 T, and down to either 1 T or to field values for which the strand critical current exceeds 1 kA (the maximum capability of power supply and current leads available at CERN). Transport $\mathrm{J_c}$ data of all strands have been corrected for a simple self-field effect:

$$B_{total} = B_{external} + B_{self-field} = B_{external} + \frac{\mu_0 I_c}{2\pi R_{fil}} \quad (1)$$

where R_{fil} is the radius of the filamentary region within the strand.

The low-field behavior of the critical current density can be obtained by inductive measurements. Magnetization measurements have been performed by using an Oxford Instruments Vibrating Sample Magnetometer (VSM) equipped with a 12 T magnet and a 4 K–300 K variable temperature insert. The samples, whose length is of the order of few mm, were straight specimens mounted on the sample holder perpendicularly to the background field. The magnetic moment was measured as a function of field for cycles of various amplitude, between a minimum field $\mathrm{B_{min}}$ (-2 T) and a maximum field $\mathrm{B_{max}}$ (12 T at 4.2 K). To eliminate the effect of coupling currents, the cycling field ramp-rate was kept low (8 mT/s).

Critical current densities are obtained through the Bean model formula for a superconducting cylinder [7], [8]:

$$J_c^{magn}\,[\mathrm{A/cm^2}] = \frac{30\pi}{4}\frac{\Delta m\,[\mathrm{emu/cm^3}]}{d_{eff}\,[\mathrm{cm}]}(1-\lambda) \quad (2)$$

in which an effective diameter, d_{eff}, is used to scale the $\mathrm{J_c^{magn}}$ curves to the transport currents, $\mathrm{J_c^{transp}}$.

IV. Results

Fig. 1 shows both $\mathrm{J_c^{magn}}$ curves and $\mathrm{J_c^{transp}}$ data as a function of the external applied field; data are reported only at 4.2 K for the sake of simplicity. There is a good match between magnetic and transport measurements; also, a very good agreement between CERN and ENEA data is found. For Luv-NMR only transport data are available at 4.2 K.

From the magnetization cycles it is possible to determine the irreversibility field values, $\mathrm{B_{irr}}$, at the loop closure. The correlation between the low-field $\mathrm{J_c}$ and $\mathrm{B_{irr}}$ can be clearly seen in Fig. 2, in which the $\mathrm{J_c}$ at 2 T are reported as a function of $\mathrm{B_{irr}}$ at different temperatures, for all measured samples. It is interesting to note that, in general, the higher the $\mathrm{B_{irr}}$, the lower the low-field $\mathrm{J_c}$.

For all strands, we have fitted the experimental $\mathrm{B_{irr}}$ data to the Lubell formula [9], $\mathrm{B_{c2}(T) = B_{c20}[1-(T/T_{c0})^{1.7}]}$, where $\mathrm{T_{c0}}$ is the critical temperature at zero magnetic flux, and $\mathrm{B_{c20}}$ is the upper critical magnetic flux at zero temperature.

The critical current densities of Fig. 1 can be fitted to a 2-components model, as described in [10]:

$$J_c(B,T) = \frac{C_0}{B}(1-t^n)^\gamma \cdot\left(\delta\frac{b^{\alpha 1}(1-b)^{\beta 1}}{g(\alpha_1,\beta_1)} + (1-\delta)\frac{b^{\alpha 2}(1-b)^{\beta 2}}{g(\alpha_2,\beta_2)}\right), \quad (3a)$$

$$g(\alpha,\beta) = \left(\frac{\alpha}{\alpha+\beta}\right)^\alpha\left(\frac{\beta}{\alpha+\beta}\right)^\beta. \quad (3b)$$

where: $\mathrm{b = B/B_{c2}(T)}$ is the reduced magnetic field at a given temperature; $\mathrm{t = T/T_{c0}}$ is the reduced temperature; $\mathrm{C_0}$, α_i, β_i ($\mathrm{i} = 1,2$) are fitting parameters; n and γ are kept constant ($\mathrm{n} = 1.7, \gamma = 1.8$).

For the whole set of samples, the four parameters α_i and β_i, as well as the relative weight of the two contributions, δ, have been obtained by fitting the normalized bulk pinning forces, $\mathrm{f_p}$ vs. b, to the 2-components model, as described in [10]. Fit parameters are optimized at 4.2 K, except ITER-PF and NMR which are optimized respectively at 5.0 K and 5.1 K.

As an example of fit, the $\mathrm{f_p}$ vs. b curves are shown in Fig. 3 for sample Alst564, together with their fitting curve.

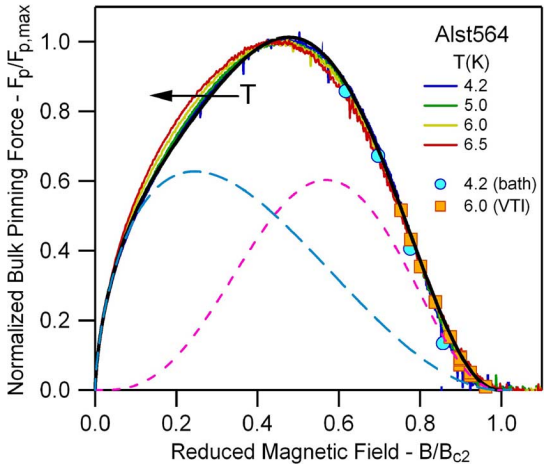

Fig. 3. Reduced pinning curves as a function of reduced field for sample Alst564. Markers represent transport data, thin lines are the magnetization data, whereas the solid thick line is the 2-components model fit. Dashed lines represent the high-field and low-field components from (3).

TABLE II
2-COMPONENTS MODEL'S FITTING PARAMETERS

Sample name	B_{c20} *(T)*	T_{c0} *(K)*	C_0 *(AT/mm²)*	α_1	β_1	α_2	β_2	δ
Alst564	15.91	8.95	27686	3.20	2.43	0.65	2.00	0.49
IBA01	14.49	8.69	37904	2.73	2.06	0.54	1.90	0.43
ICB01	14.74	8.86	34445	2.48	1.93	0.55	1.88	0.46
ITER-PF	15.05	9.27	26818	2.95	2.27	0.58	1.95	0.45
***JT-60SA*[9]**	15.19	8.91	30000	3.20	2.43	0.65	2.00	0.45
LUV-NMR	15.72	8.66	30020	2.57	1.99	0.58	1.74	0.44

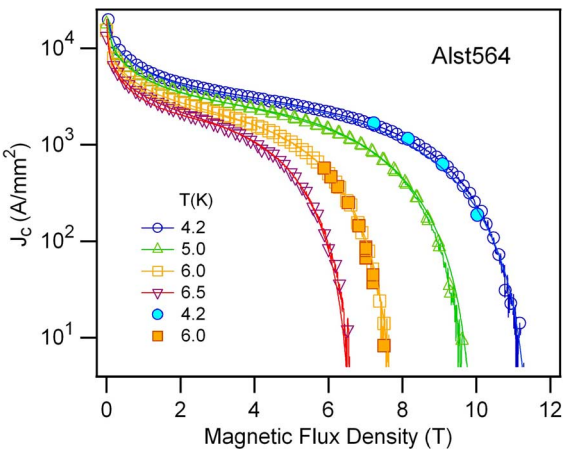

Fig. 4. Non-Cu J_c of the Alst564 strand, from magnetization (open symbols), and transport (closed symbols) measurements in the entire B, T range. Lines represents fits using (3), with the parameters listed in Table II.

Having α_i, β_i, δ, n and γ fixed, (3) can be fitted to the experimental $J_c(B,T)$ with C_0 as the only free parameter.

The whole parameter set is reported in Table II. For all strands, the 2-components model is able to describe the experimental data with good accuracy in the whole B range, and in the temperature range 4.2 K–6.5 K. As an example, in Fig. 4 the very good agreement between experimental data and fit is shown for sample Alst564.

It should be noted, finally, that the temperature dependence of $J_c(B)$ can be factorized with the same n and γ for all strands: this is an indication that the temperature behavior does not depend on the strand parameters, such as λ, d_{eff}, diameter and layout.

V. DISCUSSION

As shown in Fig. 3, the reduced pinning forces seems to scale with temperature in the investigated temperature range (4.2 K–6.5 K).

In general, a temperature scaling of f_p over a wide field and temperature range is a good indication of the fact that a single pinning mechanism is operating [11]. Scaling is not expected either if several types of pinning centers are present in the sample, or if different mechanisms with their own temperature dependencies exist for the same pinning center. This is in apparent contradiction with the results of Fig. 3. However, a slightly systematic shift of the f_p peak toward lower reduced fields is observed for increasing temperatures, for all samples. Although this lack of scaling can be barely appreciated (i.e., lies within the measurement error), the true verification of scaling requires measurements over a wider temperature range, not just in a restricted range (e. g., 4.2 K–6.5 K) [11]. In fact, the explored temperature range $(t = 0.43 - 0.65)$ is such that the BCS gap, $\Delta(t)/\Delta_0 = \tanh[(\Delta(t)/\Delta_0)/t]$ [12], vary in the range 0.98-0.87, and the non-scaling effects could be neglected. The pinning regimes and mechanisms in NbTi are complex and varied [13], so that it is difficult to provide an accurate quantitative description of the pinning mechanisms in such systems. However, bearing in mind that the 2-components formulation should be viewed as a simple model system, in the following we will try to give an explanation about the sources of these different contributions.

Two possible scenarios for the pinning mechanisms in NbTi have been proposed in literature [11], [14]. Meingast *et al.* [11] consider the idea that in optimized NbTi strands the pinning centers are clusters of α-Ti ribbons, which give rise to fluctuations in both Ginzburg-Landau parameter κ and the thermodynamic critical field H_c. Those fluctuations are responsible for the so-called $\delta\kappa$ and δH_c pinning, respectively. From the f_p curves, there is experimental evidence [11] that $\delta\kappa$ pinning leads to pinning at high reduced fields, whereas δH_c pinning leads to pinning at low reduced fields. Within this framework, in Fig. 3 the low-field pinning component could arise from δH_c pinning, whereas the high-field pinning component from $\delta\kappa$ pinning. This is also consistent with the Dew-Hughes calculations [15], for which a core-interaction pinning mechanism from a normal center would give rise to a reduced pinning force with a maximum at $b = 0.2$, whereas for a $\delta\kappa$ mechanism the maximum would lie at $b = 0.6$. As a matter of fact, as Fig. 3 shows, the two pinning mechanisms show maximum around 0.2 and 0.6 respectively.

In the other scenario proposed by Bormio-Nunes *et al.* [14], there are actually two kinds of strong pinning centers: one is the α-Ti normal interface, and the other one is identified in the Nb and Ti composition gradients around the α-Ti precipitates. Within this picture, the high-field pinning component of Fig. 3 could arise from such gradients. The high-field pinning component in (3) could also be associated to the Ti-rich film around

most of the grain boundaries [16], [17], rather than from the Nb composition gradients around the α-Ti precipitates. In this sense, although the grain boundaries density is lower than that of precipitates, it could play a not negligible role in such systems.

From our measurements, it is not possible to extract a more detailed insight into those mechanisms ruling pinning inside NbTi wires. More measurements are needed in view of obtaining an exhaustive comprehension of the behavior of those strands. In particular, it is essential to extend the measurements over a wider temperature range, in order to verify that the observed small systematic shift of the f_p peak toward lower reduced fields is definitely to be ascribed to a lack of scaling. In addition, dedicated heat treatments (HTs) [14] will be applied, in order to support the identification of the pinning mechanisms. Even if the microstructure variations due to HT seem to have no effects on J_c at high temperatures and high fields [18], the HT could modify the relative weight (δ in (3)) of the two components in the overall pinning force. TEM analyses will be performed before and after those dedicated HTs, in order to get a deeper insight of NbTi morphological characteristics, such as α-Ti ribbons clusters and grain boundaries thickness, separation, circumference and cross sectional area.

ACKNOWLEDGMENT

The authors thank Giuseppe Celentano and Andrea Augieri (ENEA) for fruitful discussions, Angelo Bonasia and Pierre Jacquot (CERN) for the sample preparation and measurements at CERN, and acknowledge David Larbalestier (NHMFL) for useful suggestions about the follow-up of our work.

REFERENCES

[1] L. Pizzuto *et al.*, "JT-60SA toroidal field magnet system," *IEEE Trans. Appl. Supercond.*, vol. 18, no. 2, p. 505, Jun. 2008.

[2] L. Muzzi *et al.*, "The JT-60SA toroidal field conductor reference sample: Manufacturing and test results," *IEEE Trans. Appl. Supercond.*, 2009, submitted for publication.

[3] L. Bottura, "Measurement of critical current and magnetization in ITER-relevant Nb-Ti strands," 2008, CERN-ITER Collaboration Report.

[4] D. Bessette *et al.*, "Test results from the PF conductor insert coil and implications for the ITER PF system," *IEEE Trans. Appl. Supercond.*, vol. 19, no. 3, pp. 1525–1531, Jun. 2009.

[5] L. Affinito *et al.*, "Variable-Temperature characterization of NbTi strands in the low critical-current density range," *J. Phys.: Conf. Ser.*, vol. 97, p. 012306, 2008.

[6] T. Boutboul, C.-H. Denarié, Z. Charifoulline, L. Oberli, and D. Richter, Critical current test facilities for LHC superconducting NbTi cable strands CERN, LHC Project Report 520, 2001.

[7] C. P. Bean, "Magnetization of hard superconductors," *Phys. Rev. Lett.*, vol. 8, p. 250, 1962.

[8] C. P. Bean, "Magnetization of high-field superconductors," *Rev. Mod. Phys.*, vol. 36, p. 31, 1964.

[9] M. S. Lubell, "Empirical scaling formulas for critical current and critical fields for commercial NbTi," *IEEE Trans. Magn.*, vol. Mag-19, no. 3, May 1983.

[10] L. Muzzi *et al.*, "Magnetic and transport characterization of NbTi strands as a basis for the design of fusion magnets," *IEEE Trans. Appl. Supercond.*, vol. 19, no. 3, pp. 2544–2547, Jun. 2009.

[11] C. Meingast and D. C. Larbalestier, "Quantitative description of a very high critical current density Nb-Ti superconductor during its final optimization strain. II. Flux pinning mechanisms," *J. Appl. Phys.*, vol. 66, no. 12, pp. 5971–5983, December 15, 1989.

[12] G. Burns, *Solid State Physics*. London: Academic Press, 1985, p. 649.

[13] L. D. Cooley, P. J. Lee, and D. C. Larbalestier, "Flux-pinning mechanism of proximity-coupled planar defects in conventional superconductors: Evidence that magnetic pinning is the dominant mechanism in niobium-titanium alloy," *Phys. Rev. B*, vol. 53, pp. 6638–6652, 1996.

[14] C. Bormio-Nunes, M. J. R. Sandim, and L. Ghivelder, "Composition gradient as a source of pinning in Nb-Ti and NbTa-Ti superconductors," *J. Phys.: Condens. Matter*, vol. 19, pp. 446204–446210, 2007.

[15] D. Dew-Hughes, "Flux pinning mechanisms in type II superconductors," *Phil. Mag.*, vol. 30, no. 2, pp. 293–305, August 1974.

[16] C. Meingast, P. J. Lee, and D. C. Larbalestier, "Quantitative description of a very high Jc Nb-Ti superconductor during its final optimization strain: I. Microstructure, Tc, Hc2, and resistivity," *J. Appl. Phys.*, vol. 66, no. 12, pp. 5962–5970, Dec. 15, 1989.

[17] D. C. Larbalestier and A. W. West, "New perspectives on flux pinning in Niobium-Titanium composite superconductors," *Acta Metall.*, vol. 32, p. 1871, 1984.

[18] A. K. Shikov *et al.*, "The effect of thermo-mechanical treatments on Jc(T,B) and Tcs of Nb-Ti strands," *IEEE Trans. Appl. Supercond.*, vol. 19, no. 3, pp. 2540–2543, 2009.